scientific reports

Check for updates

OPEN

Bare finger tactile sensing for edge orientation and contact position using excitation from fingernail

Shoha Kon[1]✉, Keigo Ushiyama[1,2], Izumi Mizoguchi[1] & Hiroyuki Kajimoto[1]

In recording and reproducing skills involving the fingertips, a sensor that measures tactile information of fingertips is important. However, when the sensor covers the finger pad, the inherent sense of touch is compromised. We introduce a new tactile sensor, a pair of a vibration motor and a 6 degrees-of-freedom sensor attached to a fingernail that enables tactile sensing without covering the fingertip. This sensor estimates finger contact information by measuring vibrations caused by an eccentric motor positioned on the fingernail. The time series of the acquired angular velocity and acceleration data were utilized to identify the edge orientation and the contact position of the touching object. The results of the conducted experiments indicated that this setup can simultaneously identify both the edge orientation and the contact position with an accuracy of 71.67%. Potential applications include remote tactile transmission, integration with a robotic finger, and the detection of grasping postures in real objects.

Keywords Active sensing, Excitation, Fingertips

Tactile sensation plays a critical role in various dexterous actions people perform with their hands. For instance, people can manipulate objects such as pencils or toothpicks without relying on visual input. However, performing the same task is more challenging when using a plastic finger cap. In such cases, people rely on tactile feedback to determine the position and orientation of the object they are handling.

If tactile information related to such dexterous operations can be recorded and transmitted remotely, the individual performing the task could act as a remote agent, facilitating remote work with tactile input. Additionally, recording tactile sensations during fine motor tasks could provide valuable insights for developing robots with dexterous manipulation capabilities[1–3].

Recording tactile sensations during manipulation generally requires wearable sensors. Many wearable tactile sensors exist, with most designed as gloves[4–6]. However, gloves interfere with the natural sense of touch by covering the fingers. Although thin-film sensors have been proposed[7–9], they often raise concerns about durability.

On the other hand, wearable tactile sensors that do not cover the finger pad have also been developed. These include sensors that detect fingernail color changes[10–12], nail deformation[13], and deformation of the side of the finger[14]. While these sensors are capable of measuring force, including its direction, they do not provide sufficient information about the contact location or shape of the object interacting with the finger.

The proposed method in this study is shown in Fig. 1, along with the coordinate system used in this paper. The tactile sensor consists of a vibration motor and a 6-degrees-of-freedom (DOF) sensor (acceleration and angular velocity sensors) mounted on the fingernail. The vibration motor generates vibrations, which are detected by the nearby 6-DOF sensor. When the finger makes contact with an object, the contact's position and shape prevent vibration along specific axes. For instance, as illustrated in Fig. 1, when the finger touches an edge in the lateral (X-axis) direction, the back-and-forth sway of the finger (rotation around the X-axis) remains unaffected. However, the side-to-side sway (rotation around the Y-axis) is disrupted. By analyzing these changes in vibration, the system can estimate the contact position and shape. The vibration motor utilized in this setup is an eccentric motor, which simplifies the estimation process by providing two degrees of vibration freedom.

This proposal does not present a perfect tactile sensing method. For example, when touching a board with a punch hole, detecting the hole might be challenging. Nevertheless, this study introduces a new area of wearable tactile sensors. Figure 2 provides a functional classification of wearable tactile sensors. In the case of a convex shape of letter 'A', (a) refers to matrix-type sensors capable of recognizing the contact object's shape,

[1]Department of Informatics, Graduate School of Informatics and Engineering, The University of Electro-Communications, 1-5-1 Chofugaoka, Chofu, Tokyo 182-8585, Japan. [2]Japan Society for the Promotion of Science (JSPS), Chiyoda, Japan. ✉email: shoha.kon@kaji-lab.jp

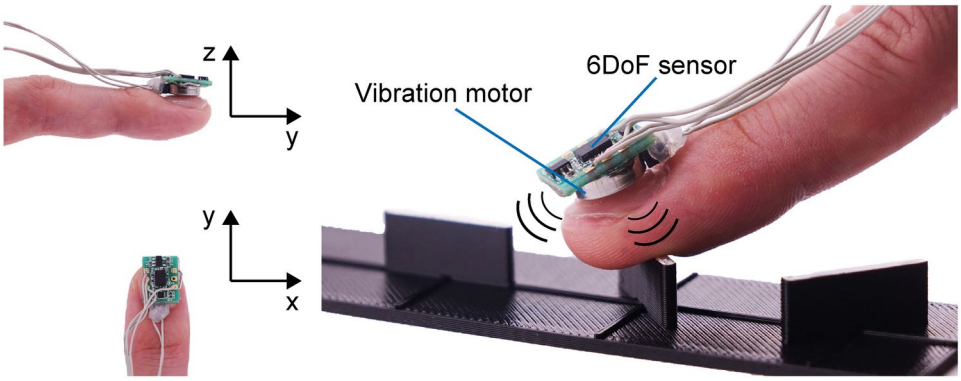

Fig. 1. Proposed method. A vibration motor and a 6-DOF sensor are attached to the fingernail. The motor induces vibrations, and the sensor captures changes caused by contact.

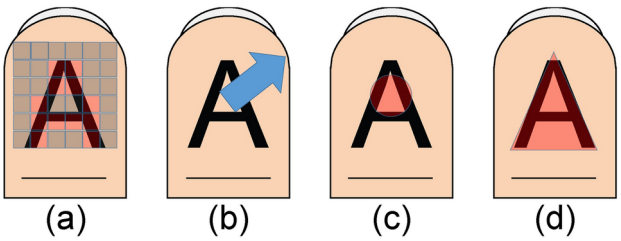

Fig. 2. Functional classification of wearable tactile sensors.

which includes glove-type sensors. (b) represents sensors that detect force direction and magnitude, such as sensors that detect nail color changes. (c) shows sensors that detect the center of gravity of the contact, and (d) detects the outer edge, although conventional wearable tactile sensors rarely address these areas. For tasks like manipulating a pencil or toothpick, understanding contact position and edge orientation is important, and this study focuses on these areas.

We propose a wearable tactile sensor that does not cover the finger pad and enables the user to detect the contact position and edges. The key contributions of this paper are as follows:

- Demonstrating that using a vibration motor and 6-DOF sensor allows for estimating the edge and contact position without covering the finger pad.
- Showing that this method can estimate both the shape of an edge and the contact position simultaneously.
- Making it clear that whether all of the data from the 6-DOF sensor is required for estimating edge shape and contact position, or whether partial data are sufficient for identification.

Related work

Our research focuses on active sensing in the tactile field, particularly wearable tactile sensors and vibration-based active sensing, which we will introduce here.

Wearable tactile sensor

Many tactile sensing techniques have been proposed to replicate the properties of human skin. Some sensors can measure skin temperature[15,16], contact force[17–19], or both[20]. The types of sensors include capacitive[21–23], piezoelectric[24], and piezoresistive[25–27]. One of the factors contributing to these advances in tactile sensing technology is the rise of flexible substrate, which are lightweight, thin, and bendable, allowing the hand to move freely without restriction[28]. In particular, ultra-thin sensors that adhere to the skin[29,30] allow for precise sensing without impeding natural skin movement. However, these sensors must cover the skin surface, which interferes with the sense of touch during object interaction.

Tactile sensor without finger pad coverage

Several approaches have been developed to acquire information about contact objects without the need to cover the finger pad. One such method involves detecting changes in nail color. Fallahinia[12] measured grip force by detecting nail color changes using deep neural networks. Abu-Khalaf et al.[10] employed a stretchable board that adapts independently of fingertip shape, while Ando et al.[11] developed a wearable fingernail sensor designed for augmented reality applications. Sakuma et al.[13] proposed a method for identifying complex human actions by capturing fingernail deformations. Sathe et al.[14] measured contact force and joint angle by measuring

the deformation of the human skin on the sides of the finger. Funato et al.[31] estimated contact 3-axis force by examining bone-conduction sounds produced by transducers attached to the phalanges of the hand.

These studies all demonstrated effective techniques for gathering tactile information without covering the finger pad. As noted earlier, these methods are well-suited for estimating the direction and magnitude of force as outlined in the functional classification of wearable tactile sensors (Fig. 2b).

Finger skin ability to detect direction of force

The ability to perceive the direction of force applied to the skin of the human fingertip is critical for recognizing both the contact position and the outer edge. Bensmaia et al.[32] demonstrated that humans are particularly sensitive to the direction of tactile stimuli, especially at reference angles like 0° and 90°. Birznieks et al.[33] reported that peripheral mechanoreceptors around nail actively respond to directional forces applied to the finger pad. Similar investigations into edge direction recognition have been conducted using robotic systems; Rongala et al.[34] employed a piezoresistive sensor array on a robotic finger to identify the direction of each edge by measuring the pressure distribution when tracing the surface of the edge in different directions.

Active sensing using vibration

In many Human-Computer Interaction (HCI) studies, various methods have been proposed to detect contact position using a combination of vibration input and measurement. For instance, GripSense[35] utilizes a smartphone's built-in vibration motor and an angular velocity sensor to estimate grasping posture. VibPress[36] applies vibration damping to estimate the pressing force and identify whether the user is pressing from the side.

Several studies have explored contact sensing on various body parts. Li et al.[37] developed authentication system for users by using vibration through their head. Liu et al.[38] detected the face touch by analyzing vibrations transmitted from the hand, while FingerPing[39] employed a speaker on the finger and multiple microphones on the wrist for gesture recognition.

Similar methods can be used for sensing including the environment. Konishi et al.[40] utilizes a speaker and a microphone to conduct user authentication when the door handle grasped. VersaTouch[41] identifies fingertip position by analyzing vibrations from multiple vibration motor on a desk. VibroScale[42] repurposes a smartphone as a weight scale by inducing vibrations, and Ali et al.[43] leverage smartphone vibrations to infer the object beneath it. Dementyev et al.[44] demonstrated that similar active sensing can be achieved using the back EMF of a vibrator, eliminating the need for separate vibration sensors.

Vibration-based active sensing in HCI is primarily applied to grasping, detecting body-to-body contact, and interaction sensing with objects on a desk. There are, however, few examples of finger-worn sensors. VibEye[45], for instance, is a finger-mounted sensor that utilizes a vibration motor and accelerometer to identify the material of an object by analyzing vibration propagation during grasping. However, while effective in identifying material types, it does not estimate other contact information.

In robotics, there are several examples of vibration-based active sensing for contact position, with a focus on its use in robotic fingers. Backus et al.[46] proposed a method to estimate contact position by vibrating the robot finger joint, identifying the resonance frequency through Phase-Lock-Loop control, and deriving the contact position from this frequency. Mitra et al.[47] also presented a method to identify contact position by measuring the vibration input and the resulting resonance frequency.

System

Figure 1 provides an overview of the device and its XYZ axis definitions. In the proposed method, both the vibration motor and the sensor are mounted on the nail side, ensuring that the finger pad is not obstructed. The vibration motor is a disk-type brushless motor (LBV10B-009, Nidec), and the sensor is a 9-DOF sensor (BMX055, BOSCH), primarily used to measure acceleration and angular velocity (only utilized 6-DOF data here). These components are affixed using double-sided tape (#1522H, 3M), with the vibration motor securely attached to the nail using high-strength tape (Kalolary) typically used for false nails. The total weight of the device affixed to the nail is approximately 2 g.

Control and measurement are managed by a microprocessor (ESP32 DevkitC, Espressif Systems). I2C communication is employed between the sensor and the microprocessor, facilitating the measurement of acceleration and angular velocity at approximately 1.4 kHz. The PC communicates with the microprocessor via a serial interface, handling data acquisition, visualization, and calculations in a Python environment.

A pseudo-DC voltage is applied to the motor using a 20 kHz PWM signal. During the experiments, the motor operated at a frequency of 169 Hz (measurement results as Supplementary Fig. 1), with the accelerometer recording a maximum acceleration of around 2.0 G. The angular velocity sensor measured a maximum angular velocity of 250 deg/s.

The proposed method employs an accelerometer and an angular velocity sensor, and a brushless vibration motor, which are expected to experience negligible effects from atmospheric pressure under standard operating conditions. In contrast, environments with extreme humidity may contribute to the degradation of electronic components in this wearable tactile sensor. This sensor operate effectively within a temperature range of − 40 to 85 °C and exhibit sensing variations of ± 0.03%/K. Such variations are unlikely to meaningfully impact the sensor's overall performance, ensuring reliability across diverse environmental conditions. The acceleration and angular velocity sensor utilized in this study operates without the need for prior calibration, and its accuracy remains unaffected by this condition.

Preliminary observation

A preliminary study was conducted by acquiring 6-DOF sensor signals and generating scatter plots for two of these signals. This preliminary observation was conducted by a single author. These scatter plots were used to

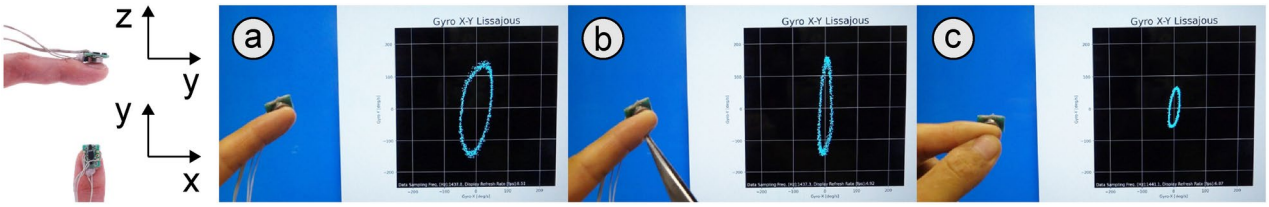

Fig. 3. Scatter diagram with X–Y axis angular velocity. (**a**) non-contact, (**b**) contact with the finger pad, (**c**) strong pressure with the finger.

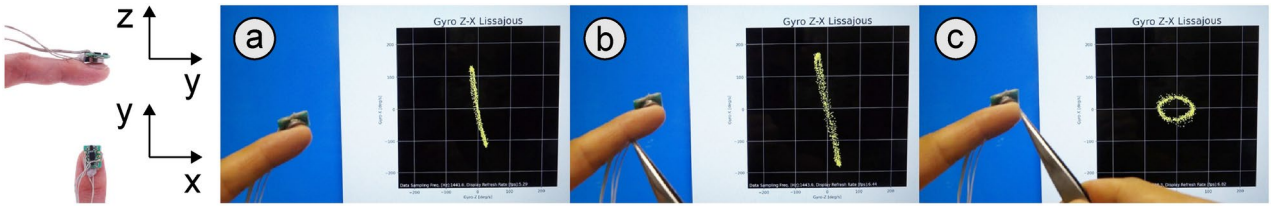

Fig. 4. Scatter diagram with Z–X axis angular velocity. (**a**) non-contact, (**b**) contact near the first joint, (**c**) contact at the finger end.

clearly observe the phase difference between two signals of the same period. If the signals were ideal sinusoidal waveforms, the scatter plot would form an oval shape. The scatter plots demonstrated robustness to variations in vibration frequency. The six sensor value combinations were considered: X–Y axis acceleration, Y–Z axis acceleration, Z–X axis acceleration, X–Y axis angular velocity, Y–Z axis angular velocity, and Z–X axis angular velocity. Some typical examples are provided below.

Figure 3 demonstrates the changes in scatter plots with X–Y axis angular velocity (see Supplementary Movie 1). (a) When the finger is not in contact with anything, the plot forms an ellipse, with angular velocity around the Y axis exceeding that of the X axis, potentially due to the finger's inherent rotational characteristics. (b) When an object (the tip of a tweezers was used here) is in contact with the finger pad, the ellipse shrinks in the direction of the X axis. (c) With increased pressure applied to the finger, the scatter diagram becomes smaller as a whole. This is thought to be because vibrations are absorbed more, suggesting that information on contact area or contact pressure can also be obtained.

Figure 4 illustrates the changes in scatter plots with Z–X axis angular velocity (see Supplementary Movie 2). (a) Without contact, the angular velocity around the Z axis is larger than that around the X axis. (b) When contact occurs near the first joint of the finger, the plot extends along the X axis. (c) Contact with the hemispherical part of the finger's end results in a near-circular plot, suggesting that these changes may enable the estimation of contact location along the anterior-posterior direction of the finger.

Learning procedure

The data processing simplifies the problem of identifying the shape and position of edges to a task of classifying vector data derived from physical contact with an object. This study employed machine learning to design an algorithm for identifying contact target patterns based on 3-axis acceleration and angular velocity data. As outlined in Fig. 5, the method for extracting vector data from a scatter diagram involves converting data points (x_n, y_n) into polar coordinates (r, θ), where:

$$r = \sqrt{x_n^2 + y_n^2}, \quad \theta = \arctan\left(\frac{y_n}{x_n}\right). \tag{1}$$

For this analysis, 1024 data points were utilized, and the sensing period of 1.4 kHz allowed data collection in approximately 0.7 s. To counteract gravitational offset, the average acceleration was subtracted. The range of θ (0° to 360°) is divided into 36 bins, each representing an interval of 10°:

$$\Delta\theta_m = [\theta_m, \theta_{m+1}), \quad \text{where} \quad \theta_m = m \times 10^\circ,\ m \in [0, 35]. \tag{2}$$

For each interval $\Delta\theta_m$, the value of $r(\theta_m)$ is calculated as the total number of points within that angular range:

$$r(\theta_m) = \sum_{i:\theta_i \in \Delta\theta_m} 1. \tag{3}$$

This results in a vector containing 36 data points for each scatter plot. This vector is represented as:

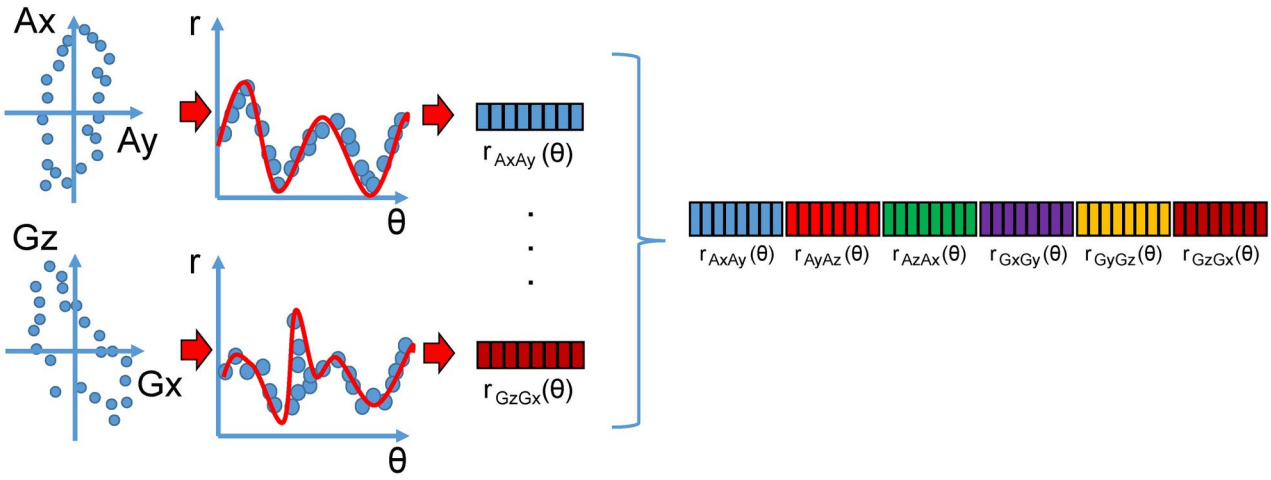

Fig. 5. Procedure for obtaining a vector from a 6-pair scatter plot.

$$\mathrm{r} = [r(\theta_0), r(\theta_1), \ldots, r(\theta_{35})]. \tag{4}$$

Six scatter plot pairs were generated from six data sets, and the resulting vectors were concatenated to produce a final vector with 216 points. These pairs—AxAy (X axis and Y axis acceleration), AyAz (Y axis and Z axis acceleration), AzAx (Z axis and X axis acceleration), GxGy (X axis and Y axis angular velocity), GyGz (Y axis and Z axis angular velocity), and GzGx (Z axis and X axis angular velocity)—collectively form the final 216-point vector:

$$\mathrm{R} = [\mathrm{r}_{AxAy}, \mathrm{r}_{AyAz}, \mathrm{r}_{AzAx}, \mathrm{r}_{GxGy}, \mathrm{r}_{GyGz}, \mathrm{r}_{GzGx}]. \tag{5}$$

In the learning phase, when we classify N contact states, contacts were applied to each pattern five times, resulting in $(N + 1) \times 5$ contacts data including non-contact instances. The vector data collected from these contacts were used as training data. A Support Vector Machine (SVM) was employed for class classification, with the SVM library in Python 3 used as the training environment.

SVM is a widely used machine learning algorithm that identifies the optimal boundary, or hyperplane, to classify data into distinct categories. In this study, SVM was employed to classify the vector r, which represents processed sensor data. The hyperplane is expressed mathematically as $w \cdot x + b = 0$, where w denotes the weight vector, x represents the input data (here, r), and b is the bias term. SVM operates by maximizing the margin, which is the distance between the hyperplane and the closest data points in each class, known as support vectors. For datasets that are not linearly separable, SVM applies a kernel function to transform the data into a higher-dimensional feature space, facilitating accurate classification of the vector r. This method enables separation of contact data derived from sensor measurements.

Results

Individual estimation

Figure 6 illustrates the identification accuracy rates for the four types of edges touched, with error bars indicating the standard error of the mean accuracy rate for ten trials per participant (See Methods section for the detail of the evaluation). Horizontal axis represents the sensor pairs utilized for estimation, and vertical axis represents the percentage of correct answers.

Independence of sensor conditions was confirmed via chi-square test ($p > 0.05$). A Shapiro–Wilk test indicated normality across all conditions, as no p-value was below 0.05. Mauchly's test for sphericity showed equal variability across groups ($p \geq 0.05$). A one-way repeated measures ANOVA on correct response rates for each sensor type revealed a significant difference ($F(8, 72) = 9.79, p = 0.00054 < 0.05$). Bonferroni post-hoc test showed significant difference between pairs:

AxAyAzGxGyGz and AxAyAz ($p = 0.025 < 0.05$), AxAyAzGxGyGz and AxAy ($p = 0.029 < 0.05$),
AxAyAzGxGyGz and AyAz ($p = 0.0059 < 0.01$), AxAyAzGxGyGz and AzAx ($p = 0.004 < 0.01$),
GxGyGz and AxAyAz ($p = 0.0048 < 0.01$), GxGyGz and AxAy ($p = 0.0015 < 0.01$),
GxGyGz and AyAz ($p = 0.0119 < 0.05$), GxGyGz and AzAx ($p = 0.0044 < 0.01$).

The highest identification accuracy was observed for the GxGyGz condition (76.75% correct response), followed closely by AxAyAzGxGyGz (74.75%). Notably, conditions using only angular velocity data (GxGy: 64.25%, GyGz: 57%, GzGx: 67.75%) outperformed those using only acceleration data (AxAy: 47.25%, AyAz: 51.25%, AzAx: 50%). The GxGyGz condition produced the highest accuracy overall. This is consistent with the fact that the motor rotation occurs around the z-axis, and finger oscillation is predominantly along the x-axes and y-axes.

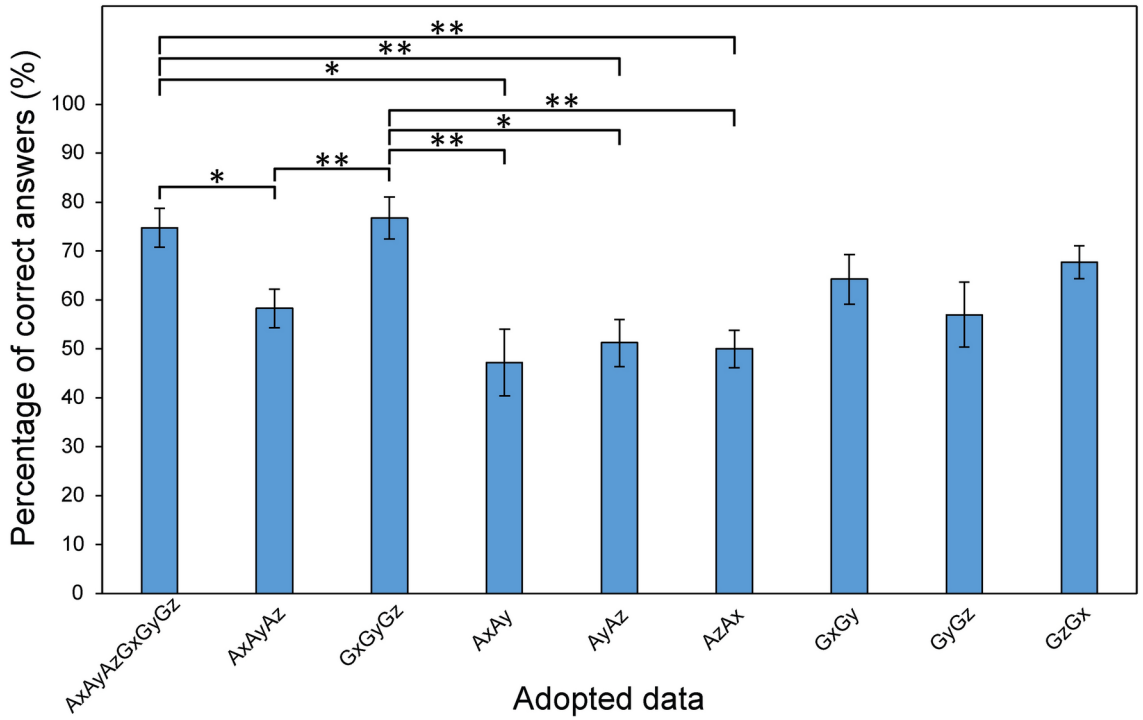

Fig. 6. Identification accuracy rates for four different edge shapes. Results for each sensor condition, along with standard errors, are presented (*: $p < 0.05$, **: $p < 0.01$). Statistical analysis was performed using one-way repeated measures ANOVA with Bonferroni correction ($n = 10$).

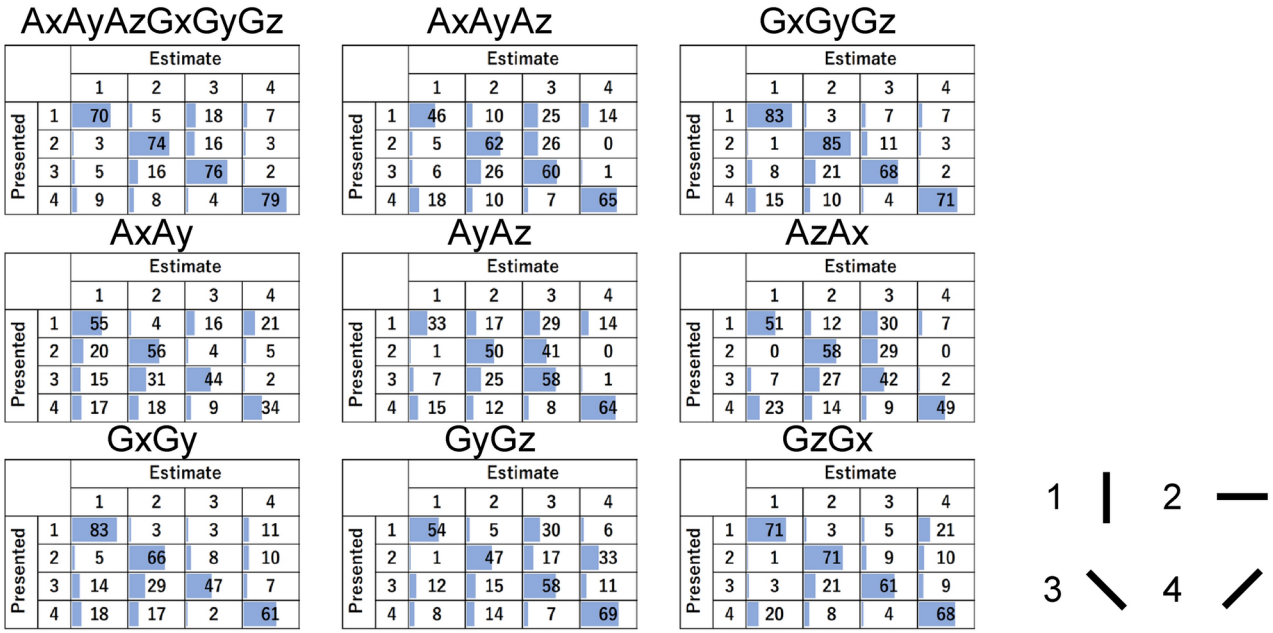

Fig. 7. Confusion Matrix of the four edge shape identification experiments, for each sensor data pair used. The numbers in the table represent percentages (%).

Figure 7 provides the confusion matrix showing the recognition results when four edges were touched (see Methods section). Pattern 1 represents a longitudinal line, pattern 2 a lateral line, pattern 3 a diagonal line from the upper left to the lower right, and pattern 4 a diagonal line from the front right to the back left. The data reveal that, across all sensor conditions, pattern 1 (longitudinal line) was most often confused with patterns 3 and 4 (diagonal lines). Pattern 2 (lateral line) was most often confused with either pattern 3 or 4 as well. For example,

in the AzAx condition, pattern 1 was never confused with pattern 2 but was confused with pattern 3 in 7% and as pattern 4 in 23%. In the GxGyGz condition, pattern 2 was confused with pattern 1 in 3%, but it was mistaken for patterns 3 and 4 in 21% and 10%, respectively. In contrast, longitudinal lines were rarely confused with lateral lines, and lateral lines were rarely confused with longitudinal lines in any condition. This is likely due to the substantial difference in contact areas between the fingers and the surface. When touching longitudinal versus lateral lines, whereas the contact areas were more similar when comparing longitudinal and diagonal lines or lateral and diagonal lines, resulting in analogous vibration patterns.

Figure 8 depicts the accuracy rates for identifying six different pins touched (see Methods section). The chi-square test confirmed the independence of the conditions ($p > 0.05$), and Mauchly's test for sphericity showed equal variability ($p \geq 0.05$). However, a Shapiro–Wilk test demonstrated non-normality in one of the nine conditions ($p = 0.016$). As a result, a Friedman test was performed to assess the correct response rates for each sensor condition ($p = 0.00037 < 0.05$), confirming a significant difference. Post-hoc analysis using the Nemenyi test identified significant differences between all conditions except for those involving the six-sensor condition (AxAyAzGxGyGz), AxAyAz, and GxGyGz. Nemenyi test also demonstrated significant differences were found between AxAyAz and AxAy ($p = 0.0024 < 0.05$), GxGyGz and AxAy ($p = 0.001 < 0.05$), GxGyGz and AzAx ($p = 0.0029 < 0.05$), and GxGyGz and GyGz ($p = 0.0012 < 0.05$). When analyzing identification accuracy rates, similar to the findings for edge identification, the condition utilizing six types of sensor data (AxAyAzGxGyGz) exhibited the highest accuracy (91.33%), followed by the condition using three angular velocity data (GxGyGz), which achieved an accuracy of 88.17%. The lowest accurate condition was AxAy, with an accuracy of 59.17%. The AxAy condition also had the lowest accuracy in the edge identification task, indicating that detecting both the shape and the contact position is challenging when relying solely on the AxAy condition.

Figure 9 provides the confusion matrix for each of the nine conditions when six different pins were touched. Pattern 1 refers to the upper-left pin, pattern 2 to the middle-left pin, pattern 3 to the lower-left pin, pattern 4 to the upper-right pin, pattern 5 to the middle-right pin, and pattern 6 to the lower-right pin. Across all conditions, pattern 5 (middle right pin) was frequently confused with pattern 6 (bottom right pin).

Simultaneous estimation

Figure 10 illustrates the identification accuracy rates for 12 distinct edges, with results displayed for each sensor information combination used. The independence of the conditions was confirmed through a chi-square test ($p > 0.05$). Mauchly's sphericity test indicated equal variance ($p \geq 0.05$), and the Shapiro–Wilk test verified normality across all conditions ($p > 0.05$). A one-way repeated measures ANOVA was applied to the percentage

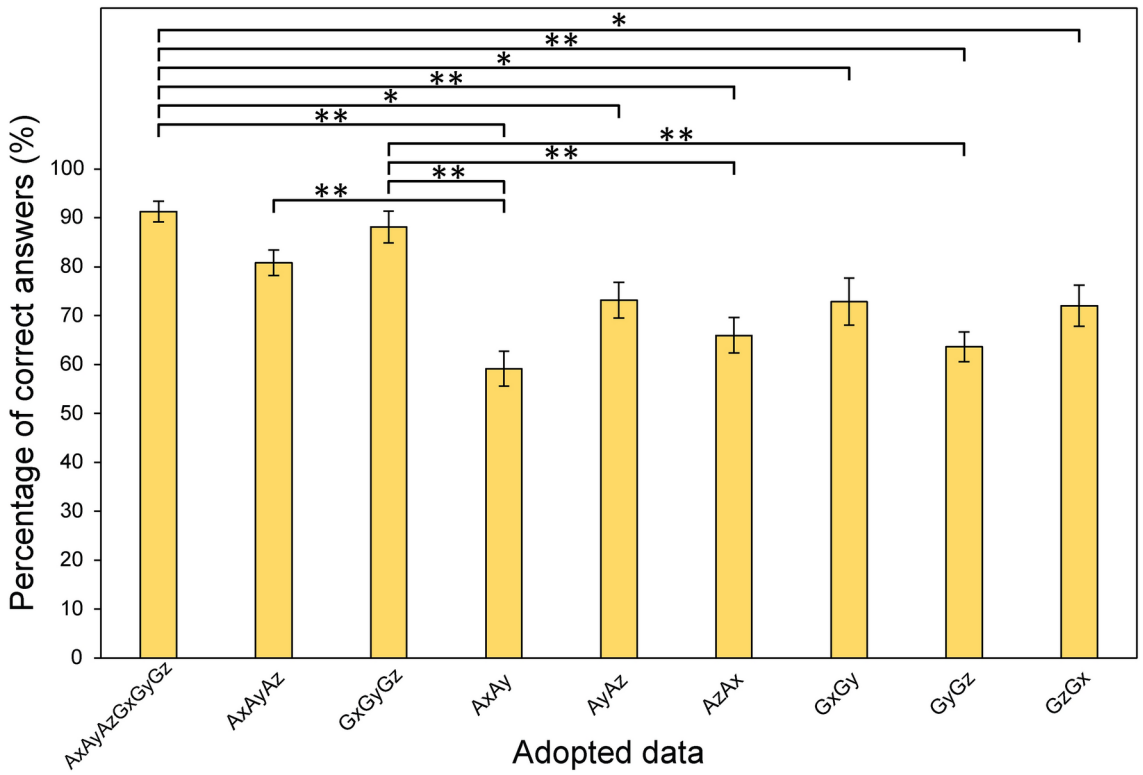

Fig. 8. Identification accuracy rates for six different pins. Results for each sensor condition, along with standard errors, are presented (*: $p < 0.05$, **: $p < 0.01$). Statistical analysis was performed using Friedman test with Nemenyi post-hoc test ($n = 10$).

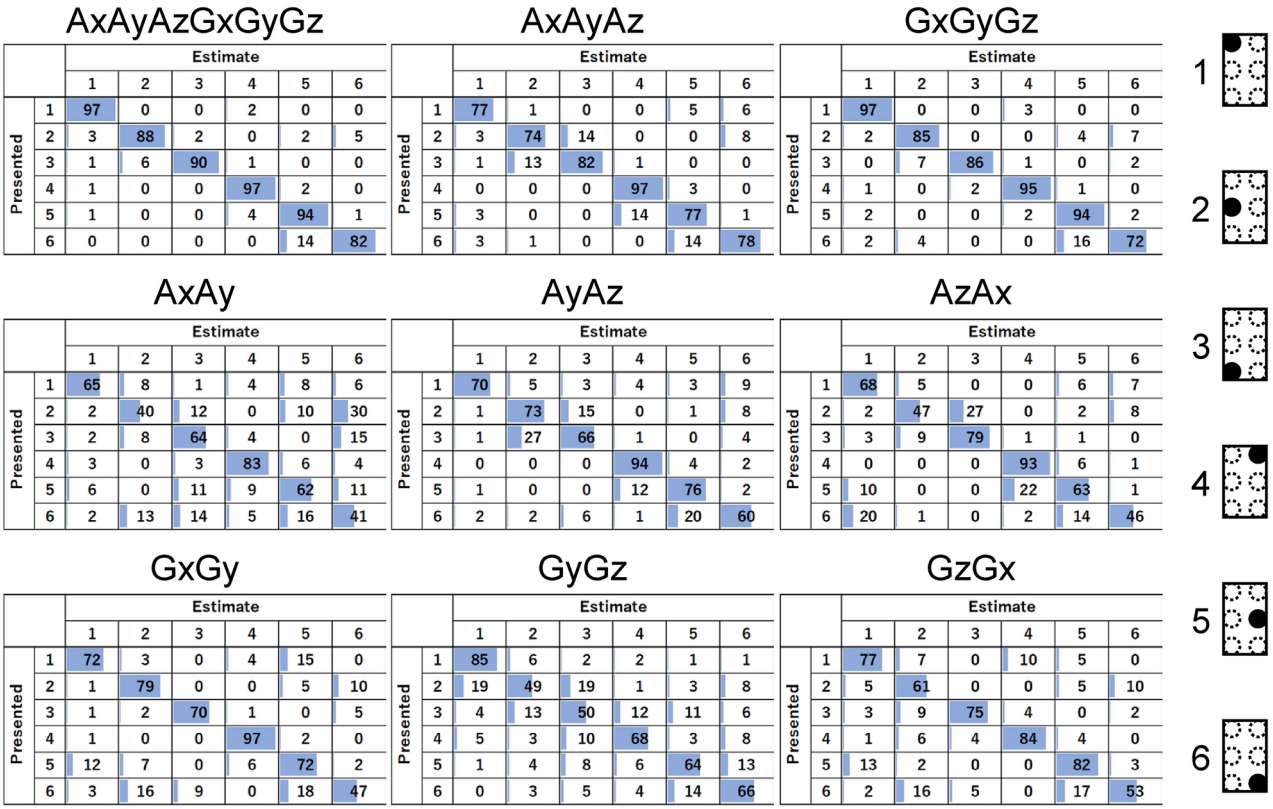

Fig. 9. Confusion Matrix of the six pins identification experiments, for each sensor data pair used. The numbers in the table represent percentages (%).

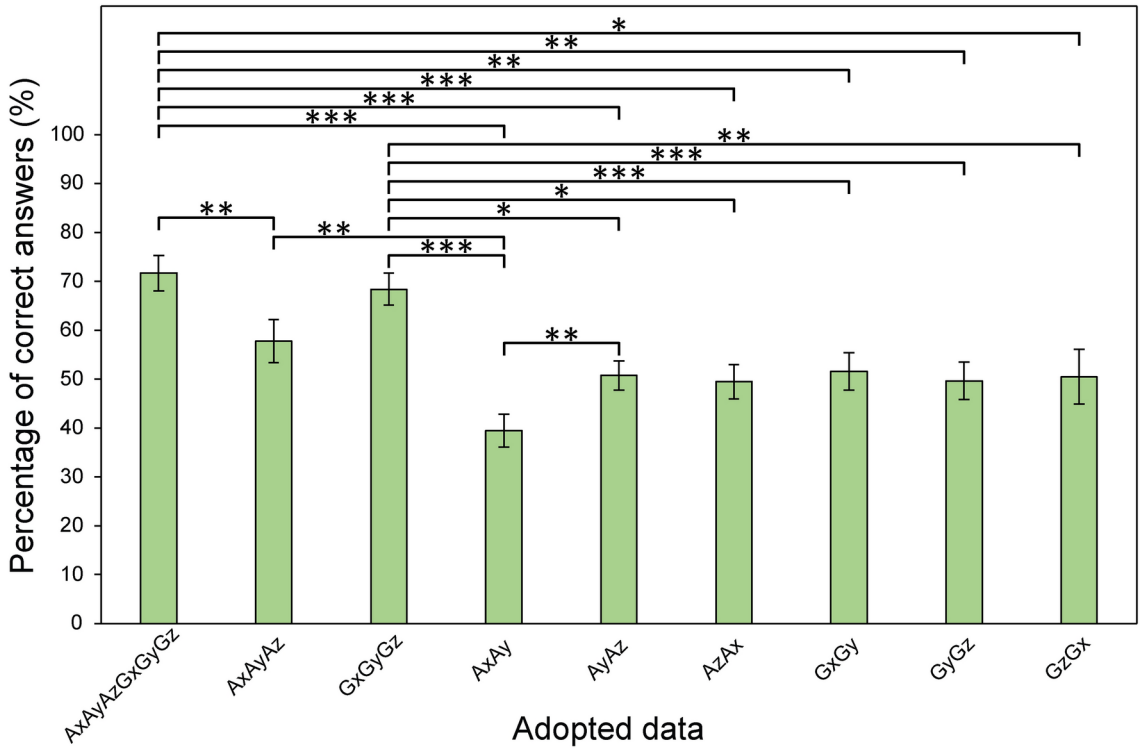

Fig. 10. Identification accuracy rates for twelve different edge shapes. Results for each sensor condition, along with standard errors, are presented (*: $p < 0.05$, **: $p < 0.01$, ***: $p < 0.001$). Statistical analysis was performed using one-way repeated measures ANOVA with Bonferroni correction ($n = 10$).

of correct responses for each sensor combination ($F(8, 72) = 17.87, p = 0.0000019 < 0.05$), revealing significant differences. Post-hoc Bonferroni analysis indicated significant differences between several conditions:

AxAyAzGxGyGz and AxAy ($p = 0.000062 < 0.001$), AxAyAzGxGyGz and AyAz ($p = 0.000089 < 0.001$), AxAyAzGxGyGz and AzAx ($p = 0.000262 < 0.001$), GxGyGz and AxAy ($p = 0.000451 < 0.001$), GxGyGz and GxGy ($p = 0.000700 < 0.001$), GxGyGz and GyGz ($p = 0.000782 < 0.001$), AxAyAzGxGyGz and GxGy ($p = 0.001723 < 0.01$), AxAyAzGxGyGz and GyGz ($p = 0.002536 < 0.01$), AxAyAzGxGyGz and AxAyAz ($p = 0.001396 < 0.01$), AxAyAz and AxAy ($p = 0.002327 < 0.01$), GxGyGz and GzGx ($p = 0.002355 < 0.01$), AxAy and AyAz ($p = 0.002601 < 0.01$), AxAyAzGxGyGz and GzGx ($p = 0.016523 < 0.05$), GxGyGz and AyAz ($p = 0.010130 < 0.05$), GxGyGz and AzAx ($p = 0.039235 < 0.05$).

The significant differences among all conditions are summarized in Fig. 10. Similar to individual estimation, the condition involving all six sensor data types (AxAyAzGxGyGz, 71.67%) and the condition using three angular velocity data types (GxGyGz, 68.4%) achieved higher accuracy than the other conditions, with accuracy rates around 70%. The AxAy condition exhibited the lowest accuracy at 39.5%. Notably, unlike in individual estimation, the angular velocity condition and the acceleration condition displayed comparable accuracy levels, each around 50%.

Figures 11 and 12 provide confusion matrix for the recognition outcomes of 12 different edge positions and shapes. Numbers 1 through 12 correspond to the edges numbered 1 to 12 in the upper-left section of Fig. 11. Confusion occurred primarily within groups "1, 2, 3, 4", "5, 6, 7, 8", and "9, 10, 11, 12". For example, edge 2 in the AxAyAzGxGyGz condition was frequently confused with edges 1, 3, and 4, while edge 6 in the GxGyGz

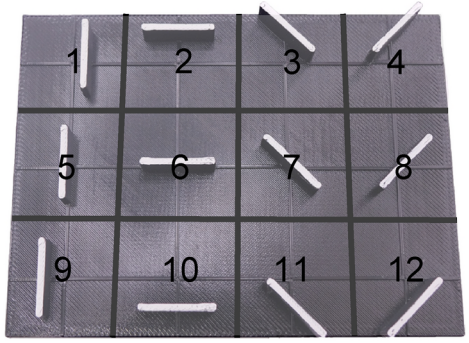

AxAyAzGxGyGz

Presented \ Estimate	1	2	3	4	5	6	7	8	9	10	11	12
1	88	1	10	0	1	0	0	0	0	0	0	0
2	0	88	5	4	0	0	3	0	0	0	0	0
3	2	4	90	3	1	0	0	0	0	0	0	0
4	0	11	2	81	2	4	0	0	0	0	0	0
5	0	2	0	0	69	7	10	7	1	0	0	0
6	0	0	0	0	5	52	22	5	3	0	7	4
7	0	0	0	0	3	28	54	9	4	0	1	1
8	0	0	0	0	14	14	6	65	0	0	0	1
9	0	0	0	0	1	0	1	0	88	0	9	1
10	0	0	0	0	0	0	0	0	0	76	8	16
11	0	0	0	0	0	0	0	0	0	34	54	12
12	0	0	0	0	0	3	0	0	1	31	9	55

AxAyAz

Presented \ Estimate	1	2	3	4	5	6	7	8	9	10	11	12
1	77	8	15	0	0	0	0	0	0	0	0	0
2	1	84	7	5	0	0	3	0	0	0	0	0
3	3	9	84	4	0	0	0	0	0	0	0	0
4	0	16	2	73	1	5	0	3	0	0	0	0
5	0	2	0	0	62	8	10	13	1	0	0	0
6	0	0	0	0	8	29	29	3	5	0	5	5
7	0	0	0	0	0	19	45	15	6	1	0	8
8	0	1	2	3	20	11	12	48	0	0	0	1
9	0	0	0	0	0	2	4	0	56	13	18	5
10	0	0	0	0	1	0	0	0	0	64	18	15
11	0	0	0	0	0	0	0	0	0	43	36	16
12	0	0	0	0	3	0	3	0	1	38	18	36

GxGyGz

Presented \ Estimate	1	2	3	4	5	6	7	8	9	10	11	12
1	71	7	14	0	2	1	2	2	0	0	1	0
2	0	85	4	9	0	0	2	0	0	0	0	0
3	1	17	72	3	3	0	4	0	0	0	0	0
4	0	5	4	85	4	0	0	1	0	0	1	0
5	5	0	0	0	76	2	4	4	9	0	0	0
6	1	0	0	0	2	67	14	8	0	0	6	1
7	1	0	0	0	8	24	54	4	3	1	4	0
8	5	0	0	0	5	21	5	61	3	0	0	0
9	0	0	0	0	10	5	11	1	67	0	2	3
10	0	0	0	0	1	3	0	0	0	78	7	10
11	0	0	0	0	3	1	2	0	0	33	57	3
12	0	0	0	0	0	11	0	0	0	32	5	48

AxAy

Presented \ Estimate	1	2	3	4	5	6	7	8	9	10	11	12
1	21	5	14	7	13	12	3	6	3	10	0	2
2	0	67	8	13	1	4	2	0	1	1	1	0
3	0	20	54	2	7	2	2	0	0	3	1	3
4	11	10	3	58	2	6	0	0	2	0	2	1
5	7	0	0	5	47	3	9	10	2	1	5	2
6	6	0	0	1	8	13	19	7	2	1	24	12
7	9	0	0	0	9	3	29	3	2	2	22	7
8	3	5	0	0	17	5	17	15	5	5	17	6
9	0	0	0	1	15	1	6	2	49	5	9	0
10	0	0	5	0	0	1	1	0	1	53	19	11
11	0	0	0	0	0	4	6	2	0	25	34	23
12	1	0	6	0	1	2	3	3	0	25	22	34

AyAz

Presented \ Estimate	1	2	3	4	5	6	7	8	9	10	11	12
1	57	19	14	5	3	0	1	1	0	0	0	0
2	3	76	10	11	0	0	0	0	0	0	0	0
3	3	15	76	5	1	0	0	0	0	0	0	0
4	0	11	5	76	0	3	1	3	0	0	0	0
5	1	5	3	1	37	6	21	10	7	2	0	0
6	1	0	0	0	9	28	22	8	0	3	7	6
7	0	0	0	1	5	10	43	11	3	5	0	8
8	0	2	0	6	19	8	13	49	0	0	0	1
9	0	0	0	0	1	2	6	0	38	14	21	15
10	0	0	0	0	0	0	3	0	0	36	44	13
11	0	0	0	0	0	0	0	0	0	18	63	15
12	0	0	0	0	0	0	6	0	3	22	33	30

Fig. 11. Confusion Matrix of the twelve edge shapes identification experiments, for each sensor data pair used (The remaining pairs are shown in Fig. 12).

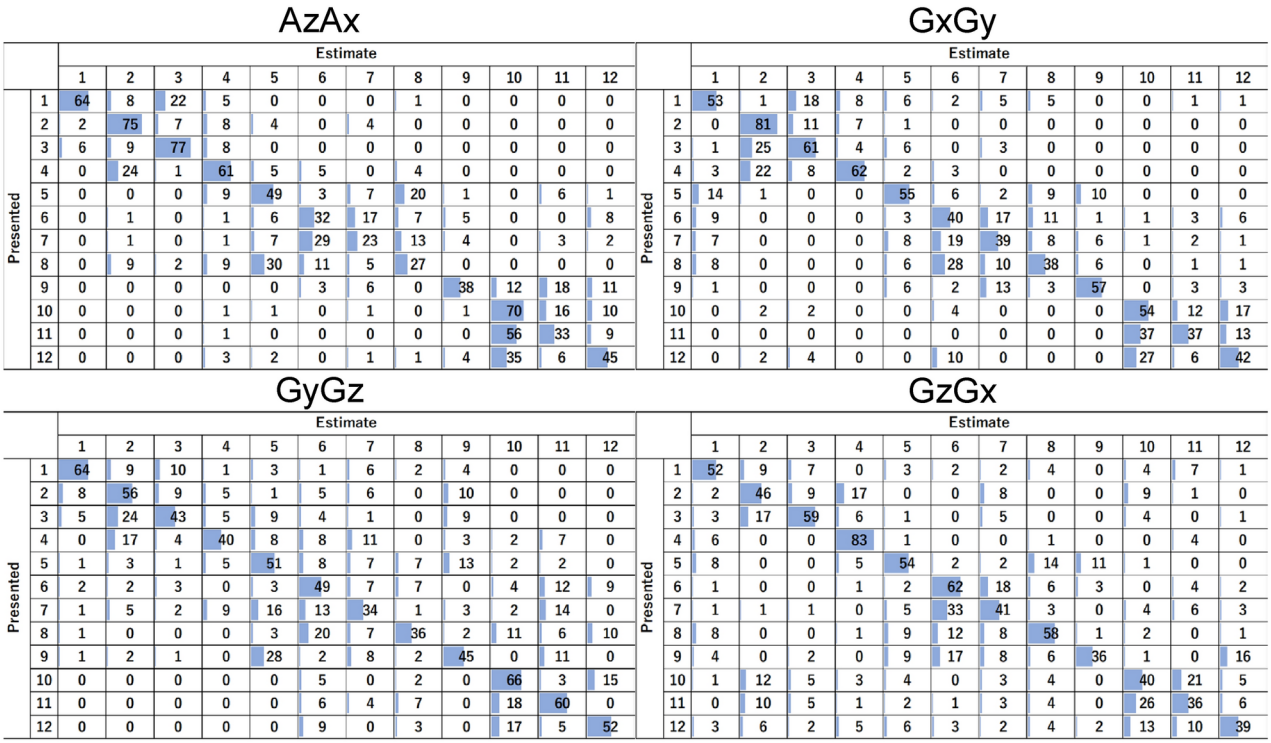

Fig. 12. Confusion Matrix of the twelve edge shapes identification experiments, for each sensor data pair used (Continued from Fig. 11).

condition was commonly mistaken for edges 7 and 8. The proposed method appears to be effective in detecting the center of gravity (e.g., "2, 6, 10", "3, 7, 11"), but less accurate in detecting edge orientation (e.g., "5, 6, 7, 8", "10, 11, 12"). This outcome aligns with the individual identification results observed in individual estimation.

Discussion

The primary goal of this study was to estimate the contact information without interfering with the inherent sense of touch by covering the fingertip. Equipped with a vibration motor and sensor on the nail side, the proposed method successfully resolved this issue by preventing the obstruction of tactile sensations caused by covering the fingertip. However, as this configuration measures vibration propagation, users still perceive vibrations from the device, which interferes with the original tactile sense. This introduces a new issue, raising concerns about the potential obstruction of tactile sensations in the finger due to vibrations.

The device provides a vibration of approximately 170 Hz, and feedback from participants indicated that the sensation was not particularly bothersome. This suggests that the vibrations from current setup are not intense to disrupt normal tactile feedback. Two possible future solutions include using either very low frequencies (around 5 Hz) to soften the stimulation or very high frequencies (up to 1 kHz) beyond the range detectable by tactile receptors. However, further research is needed to determine whether the finger can still detect vibrations effectively at these frequencies. Another potential solution is to apply vibration only at the moment of contact. As tactile sensations are primarily generated by touch, vibrations introduced only at the moment of contact would likely not interfere. For instance, at 170 Hz, each vibration cycle is 6 ms, and the shape of a contact object could be discerned after approximately 10 cycles. This setup currently collects data from about 1,000 points over 0.7 seconds using a sampling rate of 1.4 kHz. However, much less time might be required for accurate identification since one cycle of data may suffice.

Since the vibration pattern changes with each use, a learning phase is always necessary before estimation. In individual estimation, four to six contact objects were tested, with five to seven patterns collected five times each, including a no-contact condition. This process took less than five minutes, allowing users to learn the system quickly. However, as the number of objects increases, the learning time will likely grow. To address this, an actively driven pin matrix could automate the learning process. An automated data collection system would allow for more extensive datasets and could enable the use of advanced learning algorithms, such as deep learning, in addition to the SVM model used in this study.

For this new tactile sensor to be applicable in practical settings, it must be capable of estimating force amplitude in addition to contact position and edge direction. On the other hand, force amplitude estimation may be relatively straightforward. It is because the transmission of vibration is inhibited as the pressing force increases, causing the amplitude to decrease. As a result, this study did not focus on force amplitude estimation. Future research will explore whether this sensor can estimate force amplitude simultaneously with other factors.

In addition, it is not yet clear what kind of information this sensor cannot detect. For instance, in principle, if a shape is concave near the center (e.g., a ring shape in the shape of an O), the concavity in the center of the shape is considered to be undetectable. Nonetheless, as indicated in Fig. 2d, this sensor appears capable of detecting the convex outer shape of contact objects.

Although this sensor was tasked with identifying discrete patterns in this study, edge slope and contact position are continuous variables. Therefore, future training should focus on enabling the sensor to produce continuous outputs. Currently, the system assigns probabilities to patterns, with the highest-probability pattern selected as the estimate. By incorporating weighted probabilities, the proposed method may be able to provide continuous edge slope estimations.

Application

Potential application includes remote transmission of tactile sensations (Supplementary Movie 3), integration with robotic fingers (Supplementary Movie 4), and detection of object grasping postures (Supplementary Movie 5). In the remote transmission application, a user can feel the tactile feedback from what is touched by a wearing finger through an electro-tactile display. The transmitted information includes the object's edge shape and location, and it is relayed to the electro-tactile display that reproduces the tactile sensation at the receiver's end. In the robotic finger application, the device is mounted on the nail side of a 3D-printed robotic finger, mounted at the tip of robot hand (myCobot 320 Pi, Elephant Robotics). The main advantage of this setup is that it can be retrofitted to existing robotic fingers. Final application is detection of grasping postures in real objects. The orientations and positions of the edges utilized during the experiment were relatively simple. This application aimed to demonstrate that the proposed method can also be utilized in real-world grasping postures. The device was applied to an index finger grasping a screwdriver. Calibration was performed across various typical longitudinal, lateral, and diagonal grasping postures. These tests confirmed that the proposed method could detect different grasping postures. Detecting these postures is critical for recording, reproducing, and transmitting detailed movements.

Conclusion

This study introduced a new tactile sensor, a wearable tactile sensor designed to detect the contact position and the outer edge of contact objects without covering the finger pad. This sensor comprises a vibration motor and acceleration and angular velocity sensors mounted on the fingernail. The system analyzes finger behavior induced by excitation to estimate contact position and edge orientation. Acceleration and angular velocity data are paired, plotted as scatter data, and transformed into polar coordinates. The SVM algorithm was utilized for training. The experiments confirmed the effectiveness of this sensor to identify edges in different positions and orientations, achieving a 71.67% accuracy across 12 edges. High estimation accuracy was achieved when data from all three acceleration and three angular velocity axes were used, as well as when all 3 angular velocity axes were used. Future research will focus on developing algorithms to calculate pressing pressure, automating the learning process, and minimizing tactile inhibition caused by vibrations. Additionally, the sensor's utility in teleoperation scenarios involving tactile feedback will be examined.

Methods

To evaluate the validity of the proposed method, two tests were conducted to assess whether the edge direction and the contact position could be accurately estimated independently (individual estimation). On the other hand, when a pencil or pen is grasped, the shape and position of its outer edges are recognized *simultaneously*. Sensors designed to target these areas must, therefore, estimate both the direction and position of the edges at the same time. If the proposed method can achieve this, it will demonstrate practical utility. We examined whether this sensor could estimate both the direction of the edges and the contact position simultaneously (simultaneous estimation).

Data collection

All experiments were performed in accordance with institutional guidelines and regulations. The Ethics Committee of the University of Electro-Communications approved the study (approval number H24021). All participants gave their informed consent to take part in the experiments.

Subjects

Ten participants (five females, five males, nine right-handed, one left-handed) were involved in each experiment. Each participant sat in front of the contact pattern placed on the electronic scale and wore the device on the index finger of their dominant hand.

Estimation target

The contact pattern was placed on an electronic scale. The pressing force was set at 100 g, and forces ranging from 80 to 120 g ($\pm 20\%$, determined by pilot study) were considered acceptable. The relative position between the finger and the contact pattern was adjusted by aligning the red "+" marks. the center of the finger pad was considered to correspond to the central point at the base of the nail. The base of the participant's fingernail was aligned with the center of the contact pattern, indicated by a red cross in Figs. 13 and 14. The contact surface had a crosshair on its surface to mark its center, and the 6-axis sensor attached to the participant's finger featured a red line to facilitate alignment. This setup ensured that participants could accurately align their fingers with the contact pattern.

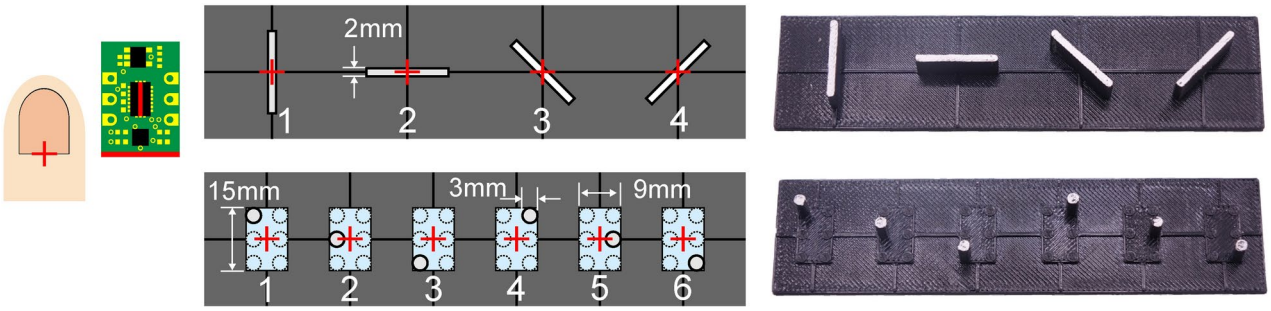

Fig. 13. Patterns utilized in individual estimation. (upper) 4 types of edge patterns, (lower) 6 types of dot patterns.

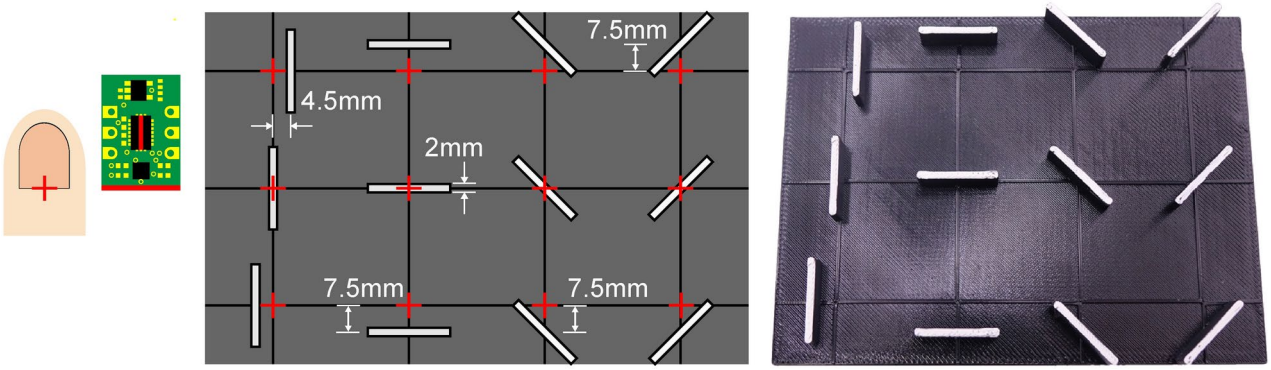

Fig. 14. Patterns utilized in simultaneous estimation.

The contact pattern utilized in individual estimation
Figure 13 provides an illustration of the contact surface utilized during the individual estimation. The first contact surface includes four edge shapes, with different angles of 45 degrees each. The second surface comprises two longitudinal rows and three lateral rows, totaling six pins, one of which protrudes. While similar to Braille, the pins have a diameter of 3 mm, and the space between adjacent pins is 6 mm, exceeding the dimensions of standard Braille. The contact area was painted white and raised 10 mm above the base to prevent accidental contact with other parts of the instrument.

The contact pattern utilized in simultaneous estimation
Figure 14 shows the contact surface utilized during the simultaneous estimation. The middle row of edges was identical to that employed in the four-way edges utilized for individual estimation, with the edge center aligned with the central axis, marked by the red "+" mark. In contrast, the edges in the top and bottom rows were offset from the central axis. For example, the top-left longitudinal edge was 4.5 mm to the right of the axis, while the bottom-right edge was positioned 7.5 mm below it. Consistent with the individual estimation, all contact areas were painted white and were 2 mm thick. The edges were 10 mm high, allowing the experiment to proceed without contact with other parts of contact surface.

Experimental procedure

The procedure is depicted in Fig. 15. The experiment included a learning phase and a test phase. After the device was properly attached to the index finger of the participant's dominant hand, participants practiced aligning positions for all trial patterns. After completing the practice, they performed the learning phase and the test phase. During the learning phase, participants were first instructed to hold their finger stationary without touching anything, and the vibration data in this state were recorded (None in Fig. 15). Subsequently, participants were instructed to sequentially touch each of the contact patterns from left to right. As for the twelve edges, participants were instructed to touch from the top row to the bottom row and from left edge to right edge (see numbering in Fig. 11). When placing their finger on each contact pattern, participants carefully aligned the red line on the sensor with the contact pattern as previously described. Vibration data for each condition were recorded in the same manner. In the test phase, participants were instructed to touch the contact patterns sequentially as with learning phase. With the device-attached finger, participants carefully aligned it with the reference line. During this process, the mode of the ten estimation results calculated using the SVM was determined, and this mode was regarded as the estimation result for the corresponding contact pattern.

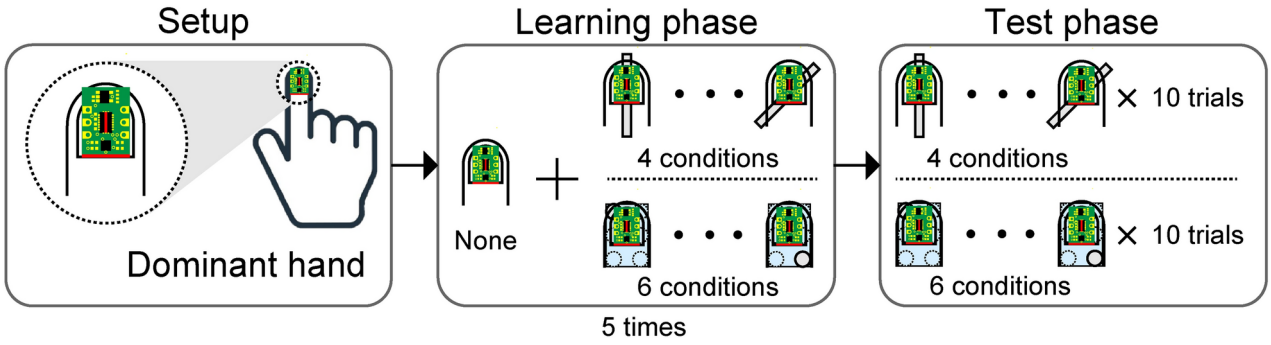

Fig. 15. Experimental procedure for individual estimation.

During the experiment, participants received instructions from the experimenter on which edge to touch next after completing contact with each edge. This ensured that participants could focus on aligning the relative position of their finger with the edge, without memorizing the order pattern.

In the experiment involving four-way edges, the learning phase consisted of five trials for five different conditions, including the non-contact condition and the four directional edges. During the test phase, participants touched the four edges sequentially, and the model's predictions were recorded. This process was repeated ten times, resulting in a total of forty datasets per single person.

In the experiment using six pins, the learning phase consisted of five trials for seven conditions, including the non-contact condition. During the test phase, data were collected as participants touched the six pins ten times, resulting in a total of sixty datasets per single person.

In the experiment involving twelve types of edges used for simultaneous estimation, the learning phase consisted of five trials for thirteen conditions, including the non-contact condition. During the test phase, vibration data were recorded as participants touched the twelve types of edges across ten rounds, resulting in a total of one hundred twenty datasets per single person.

Conditions for the utilized sensor information

This study aims to determine whether it is necessary to use all of the 6-DOF sensor data or if identification can be achieved using only part of the data. The following conditions were tested simultaneously during the estimation:

- Using all 6-DOF sensor values (AxAyAzGxGyGz condition)
- Using all acceleration sensor values (AxAyAz condition)
- Using all angular rate sensor values (GxGyGz condition)
- Using acceleration values along the x-axis and y-axis directions (AxAy condition)
- Using acceleration values along the y-axis and z-axis directions (AyAz condition)
- Using acceleration values along the z-axis and x-axis (AzAx condition)
- Using angular velocity values around the x-axis and y-axis (GxGy condition)
- Using angular velocity values around the y-axis and z-axis (GyGz condition)
- Using angular velocity values around the z-axis and x-axis (GzGx condition)

AxAyAzGxGyGz condition employed the method outlined in the previous section (Fig. 5). For AxAyAz condition, for example, three vectors were derived from the scatter plots of the Ax-Ay, Ay-Az, and Az-Ax pairs using the same method as before. These vectors were then combined to form a single vector. In AxAy condition, the scatter plot of Ax-Ay pairs was similarly used to generate vector data through the same process.

Data availability

The datasets generated during and/or analyzed during the current study are available from the corresponding author on reasonable request.

Received: 25 November 2024; Accepted: 24 February 2025
Published online: 03 March 2025

References

1. Lu, Z. & Yu, H. GTac-hand: A robotic hand with integrated tactile sensing and extrinsic contact sensing capabilities. *IEEE/ASME Trans. Mechatron.* **28**, 2919–2929. https://doi.org/10.1109/TMECH.2023.3264650 (2023).
2. Mu, S. et al. Dual-modal tactile e-skin: Enabling bidirectional human-robot interaction via integrated tactile perception and feedback. In *IEEE International Conference on Robotics and Automation (ICRA)*. https://doi.org/10.48550/arXiv.2402.05725 (2024).
3. Park, S., Oh, S.-R. & Hwang, D. MagTac: Magnetic six-axis force/torque fingertip tactile sensor for robotic hand applications. In *2023 IEEE International Conference on Robotics and Automation (ICRA)*, 10367–10372. https://doi.org/10.1109/ICRA48891.2023.10161042 (2023).
4. Abbass, Y., Gianoglio, C., Ali, H. A. H., Saleh, M. & Valle, M. Texture perception using tactile sensing glove based on PVDF sensors and machine learning. *IEEE Sens. Lett.* **8**, 1–4. https://doi.org/10.1109/LSENS.2024.3418500 (2024).

5. Ozioko, O. & Dahiya, R. Smart tactile gloves for haptic interaction, communication, and rehabilitation. *Adv. Intell. Syst*. https://doi.org/10.1002/aisy.202100091 (2022).
6. Pratap, S., Hatta, Y., Ito, K. & Hazarika, S. M. Understanding grasp synergies during reach-to-grasp using an instrumented data glove. *IEEE Sens. J.* https://doi.org/10.1109/JSEN.2024.3523512 (2025).
7. Su, F.-C. & Huang, H.-X. Flexible switching pressure sensors with fast response and less bending-sensitive performance applied to pain-perception-mimetic gloves. *ACS Appl. Mater. Interfaces* **15**, 56328–56336. https://doi.org/10.1021/acsami.3c13930 (2023).
8. Sharma, S. et al. Stretchable and all-directional strain-insensitive electronic glove for robotic skins and human-machine interfacing. *ACS Nano* **17**, 8355–8366 (2023).
9. Yang, C. et al. High strain-insensitive performance stretchable pressure sensor based on the laser-engraved graphene with a serpentine nested structure. *ACS Appl. Nano Mater.* **8**, 1129–1136. https://doi.org/10.1021/acsanm.4c06040 (2025).
10. Abu-Khalaf, J. M. & Mascaro, S. A. Optimization of stretchable fingernail sensor fabrication based on finite element modeling. In *2018 IEEE Sensors Applications Symposium (SAS)*, 1–6. https://doi.org/10.1109/SAS.2018.8336754 (2018).
11. Ando, H., Watanabe, J., Inami, M., Sugimoto, M. & Maeda, T. A fingernail-mounted tactile display for augmented reality systems. *Electron. Commun. Jpn. Pt.* **II**(90), 56–65. https://doi.org/10.1002/ecjb.20355 (2007).
12. Fallahinia, N. & Mascaro, S. A. Real-time tactile grasp force sensing using fingernail imaging via deep neural networks. *IEEE Robot. Autom. Lett.* **7**, 6558–6565. https://doi.org/10.1109/LRA.2022.3173751 (2022).
13. Sakuma, K. et al. Wearable nail deformation sensing for behavioral and biomechanical monitoring and human-computer interaction. *Sci. Rep.* **8**, 18031. https://doi.org/10.1038/s41598-018-36834-x (2018).
14. Sathe, P. et al. Development of exo-glove for measuring 3-axis forces acting on the human finger without obstructing natural human-object interaction. In *2020 IEEE/RSJ International Conference on Intelligent Robots and Systems (IROS)*, 4106–4113. https://doi.org/10.1109/IROS45743.2020.9341609 (2020).
15. Jo, H. S., An, S., Kwon, H.-J., Yarin, A. L. & Yoon, S. S. Transparent body-attachable multifunctional pressure, thermal, and proximity sensor and heater. *Sci. Rep.* **10**, 2701. https://doi.org/10.1038/s41598-020-59450-0 (2020).
16. Won, S. M. et al. Multimodal sensing with a three-dimensional piezoresistive structure. *ACS Nano* **13**, 10972–10979. https://doi.org/10.1021/acsnano.9b02030 (2019).
17. Battaglia, E. et al. ThimbleSense: A fingertip-wearable tactile sensor for grasp analysis. *IEEE Trans. Haptics* **9**, 121–133. https://doi.org/10.1109/TOH.2015.2482478 (2016).
18. Gao, Y. et al. Wearable microfluidic diaphragm pressure sensor for health and tactile touch monitoring. *Adv. Mater.* **29**, 1701985. https://doi.org/10.1002/adma.201701985 (2017).
19. Sathe, P. et al. Fingertac—an interchangeable and wearable tactile sensor for the fingertips of human and robot hands. In *2023 IEEE/RSJ International Conference on Intelligent Robots and Systems (IROS)*, 10813–10820. https://doi.org/10.1109/IROS55552.2023.10342285 (2023).
20. Wang, Y., Lu, Y., Mei, D. & Zhu, L. Liquid metal-based wearable tactile sensor for both temperature and contact force sensing. *IEEE Sens. J.* **21**, 1694–1703. https://doi.org/10.1109/JSEN.2020.3015949 (2021).
21. Hsieh, G.-W. & Chien, C.-Y. Wearable capacitive tactile sensor based on porous dielectric composite of polyurethane and silver nanowire. *Polymers* **15**, 3816. https://doi.org/10.3390/polym15183816 (2023).
22. Kwon, D. et al. Highly sensitive, flexible, and wearable pressure sensor based on a giant piezocapacitive effect of three-dimensional microporous elastomeric dielectric layer. *ACS Appl. Mater. Interfaces* **8**, 16922–16931. https://doi.org/10.1021/acsami.6b04225 (2016).
23. Mazzotta, A., Carlotti, M. & Mattoli, V. Conformable on-skin devices for thermo-electro-tactile stimulation: Materials, design, and fabrication. *Mater. Adv.* **2**, 1787–1820. https://doi.org/10.1039/D0MA00817F (2021).
24. Li, J., Yin, J., Wee, M. G. V., Chinnappan, A. & Ramakrishna, S. A self-powered piezoelectric nanofibrous membrane as wearable tactile sensor for human body motion monitoring and recognition. *Adv. Fiber Mater.* **5**, 1417–1430. https://doi.org/10.1007/s42765-023-00282-8 (2023).
25. Ma, Y. et al. A highly flexible and sensitive piezoresistive sensor based on MXene with greatly changed interlayer distances. *Nat. Commun.* **8**, 1207. https://doi.org/10.1038/s41467-017-01136-9 (2017).
26. Zhang, H. et al. Piezoresistive sensor with high elasticity based on 3d hybrid network of sponge@cnts@ag nps. *ACS Appl. Mater. Interfaces* **8**, 22374–22381. https://doi.org/10.1021/acsami.6b04971 (2016).
27. Zhang, Y., Zeng, J., Wang, Y. & Jiang, G. Flexible three-dimensional force tactile sensor based on velostat piezoresistive films. *Micromachines* **15**, 486. https://doi.org/10.3390/mi15040486 (2024).
28. Shao, Y., Hu, H. & Visell, Y. A wearable tactile sensor array for large area remote vibration sensing in the hand. *IEEE Sens. J.* **20**, 6612–6623. https://doi.org/10.1109/JSEN.2020.2972521 (2020).
29. Wang, S. et al. Skin electronics from scalable fabrication of an intrinsically stretchable transistor array. *Nature* **555**, 83–88. https://doi.org/10.1038/nature25494 (2018).
30. Yang, J. et al. Three-dimensional conformal graphene microstructure for flexible and highly sensitive electronic skin. *Nanotechnology* **28**, 115501. https://doi.org/10.1088/1361-6528/aa5b56 (2017).
31. Funato, N. & Takemura, K. Estimating three-axis contact force for fingertip by emitting vibration actively. In *2017 IEEE International Conference on Robotics and Biomimetics (ROBIO)*, 406–411. https://doi.org/10.1109/ROBIO.2017.8324451 (2017).
32. Bensmaia, S. J., Hsiao, S. S., Denchev, P. V., Killebrew, J. H. & Craig, J. C. The tactile perception of stimulus orientation. *Somatosens. Mot. Res.* **25**, 49–59. https://doi.org/10.1080/08990220701830662 (2008).
33. Birznieks, I., Macefield, V. G., Westling, G. & Johansson, R. S. Slowly adapting mechanoreceptors in the borders of the human fingernail encode fingertip forces. *J. Neurosci.* **29**, 9370–9379. https://doi.org/10.1523/JNEUROSCI.0143-09.2009 (2009).
34. Rongala, U. B. et al. Tactile decoding of edge orientation with artificial cuneate neurons in dynamic conditions. *Front. Neurorobot.* https://doi.org/10.3389/fnbot.2019.00044 (2019).
35. Goel, M., Wobbrock, J. & Patel, S. GripSense: Using built-in sensors to detect hand posture and pressure on commodity mobile phones. In *Proceedings of the 25th annual ACM symposium on User interface software and technology (UIST '12)*, 545–554. https://doi.org/10.1145/2380116.2380184 (2012).
36. Hwang, S., Bianchi, A. & yun Wohn, K. VibPress: Estimating pressure input using vibration absorption on mobile devices. In *Proceedings of the 15th international conference on Human-computer interaction with mobile devices and services (MobileHCI '13)*, 31–34. https://doi.org/10.1145/2493190.2493193 (2013).
37. Li, F. et al. VibHead: An authentication scheme for smart headsets through vibration. *ACM Trans. Sen. Netw.* **20**, 1–21. https://doi.org/10.1145/3614432 (2024).
38. Liu, L., Cao, Z. & Li, T. FaceTouch: Practical face touch detection with a multimodal wearable system for epidemiological surveillance. In *Proceedings of the 8th ACM/IEEE Conference on Internet of Things Design and Implementation*, 13–26. https://doi.org/10.1145/3576842.3582368 (2023).
39. Zhang, C. et al. FingerPing: Recognizing fine-grained hand poses using active acoustic on-body sensing. In *Proceedings of the 2018 CHI Conference on Human Factors in Computing Systems (CHI '18)*, 1–10. https://doi.org/10.1145/3173574.3174011 (2018).
40. Tomoki Konishi, B. S. & Choi, M. Active acoustic sensing based authentication system using a door handle. In *Proceedings of the International Conference on Mobile and Ubiquitous Multimedia*, 324–330. https://doi.org/10.1145/3701571.3701587 (2024).
41. Shi, Y., Zhang, H., Cao, J. & Nanayakkara, S. VersaTouch: A versatile plug-and-play system that enables touch interactions on everyday passive surfaces. In *Proceedings of the Augmented Humans International Conference (AHs '20)*, 1–12. https://doi.org/10.1145/3384657.3384778 (2020).

42. Zhang, S., Xu, Q., Sen, S. & Alshurafa, N. VibroScale: Turning your smartphone into a weighing scale. In *Adjunct Proceedings of the 2020 ACM International Joint Conference on Pervasive and Ubiquitous Computing and Proceedings of the 2020 ACM International Symposium on Wearable Computers (UbiComp/ISWC '20 Adjunct)*, 176–179. https://doi.org/10.1145/3410530.3414397 (2020).
43. Ali, K. & Liu, A. X. Fine-grained vibration based sensing using a smartphone. *IEEE Trans. Mob. Comput.* **21**, 3971–3985. https://doi.org/10.1109/TMC.2021.3067679 (2022).
44. Dementyev, A., Olwal, A. & Lyon, R. F. Haptics with input: Back-EMF in linear resonant actuators to enable touch, pressure and environmental awareness. In *Proceedings of the 33rd Annual ACM Symposium on User Interface Software and Technology (UIST '20)*. https://doi.org/10.1145/3379337.3415823 (2020).
45. Oh, S., Yun, G., Park, C., Kim, J. & Choi, S. VibEye: Vibration-mediated object recognition for tangible interactive applications. In *Proceedings of the 2019 CHI Conference on Human Factors in Computing Systems (CHI '19)*, 1–12. https://doi.org/10.1145/3290605.3300906 (2019).
46. Backus, S. B. & Dollar, A. M. Robust resonant frequency-based contact detection with applications in robotic reaching and grasping. *IEEE/ASME Trans. Mechatron.* **19**, 1552–1561. https://doi.org/10.1109/TMECH.2013.2287761 (2014).
47. Mitra, R. et al. Contact sensing via active oscillatory actuation. In *2020 3rd International Conference on Mechatronics, Robotics and Automation (ICMRA)*, 99–104. https://doi.org/10.1109/ICMRA51221.2020.9398364 (2020).

Acknowledgements

This work was supported by JSPS KAKENHI [Grant Numbers JP20H05957].

Author contributions

S.K., K.U., I.M., and H.K. designed the study. S.K and H.K. performed fabrication and characterization of sensors. S.K. performed the experiments. S.K. analyzed data and wrote the paper. All authors reviewed the manuscript.

Declarations

Competing interests

The authors declare no competing interests.

Additional information

Supplementary Information The online version contains supplementary material available at https://doi.org/10.1038/s41598-025-91970-5.

Correspondence and requests for materials should be addressed to S.K.

Reprints and permissions information is available at www.nature.com/reprints.

Publisher's note Springer Nature remains neutral with regard to jurisdictional claims in published maps and institutional affiliations.